

Demonstrating broadband billion-to-one contrast with the Visible Nulling Coronagraph

Brian A. Hicks^{*a}, Richard G. Lyon^a, Peter Petrone III^b, Ian J. Miller^c, Matthew R. Bolcar^a, Mark Clampin^a, Michael A. Helmbrecht^d, and Udayan Mallik^a

^aNASA Goddard Space Flight Center, Greenbelt, MD, USA;

^bSigma Space Corporation, Lanham, MD, USA;

^cLightMachinery, Inc., Ottawa, ON, Canada;

^dIris AO, Inc., Berkeley, CA, USA

ABSTRACT

The key to broadband operation of the Visible Nulling Coronagraph (VNC) is achieving a condition of quasi-achromatic destructive interference between combined beams. Here we present efforts towards meeting this goal using Fresnel rhombs in each interferometric arm as orthogonally aligned half wave phase retarders. The milestone goal of the demonstration is to achieve 1×10^{-9} contrast at $2\lambda/D$ over a 40 nm bandpass centered at 633 nm. Rhombs have been designed and fabricated, and a multi-step approach to alignment using coarse positioners for each rhomb and pair has been developed to get within range of piezo stages used for fine positioning. The previously demonstrated narrowband VNC sensing and control approach that uses a segmented deformable mirror is being adapted to broadband to include fine positioning of the piezo-mounted rhombs, all demonstrated in a low-pressure environment.

Keywords: Exoplanets, high-contrast imaging, nulling coronagraphy, wavefront sensing and control, interferometry, polarization optics

1. INTRODUCTION

Direct detection and characterization of exoplanetary systems including exoplanets, dust, and debris disks, are all goals for understanding the evolution of and search for habitable planets with liquid water, and potentially life. The Visible Nulling Coronagraph (VNC) is an approach to high-contrast imaging being developed to enable such observations at both the component and system level, having been proposed for both probe-class¹ and stratospheric balloon² missions. The VNC is essentially a Mach-Zehnder interferometer with a half wave (π radian) phase shift introduced between interfering beams to achieve a null in the symmetric ($RT + TR$) output, shifting the bright fringe to the asymmetric ($TT + R'R$) output. T and R refer to transmitted and reflected components following beam splitting and recombination and prime denotes combiner traversal reflection in the reverse direction. As an instrument, the VNC has demonstrated 10^{-9} contrast averaged over an inner to outer working angle of $1 - 4\lambda/D$ in polarized narrowband (1.2 nm FWHM) light,³ the level and separation required to detect and characterize dust, debris disks, and exo-Jupiters in nearby systems. At the system level, the VNC is a viable option for a variety of planned mission telescope architectures, including the obscured 2.4-m Wide-Field Infrared Survey Telescope (WFIRST) aperture,⁴ and in the more distant future, the Advanced Technology Large Aperture Space Telescope (ATLAST), which is currently favored to be a 10-m or greater segmented aperture.^{5,6}

Application of the VNC spans all future flight telescope architectures including filled (both on- and off-axis), segmented, and sparse aperture telescope systems. Additionally it makes use of all the available output photons for null control since the flux from the target star is conserved in the bright and dark output channels of the VNC. This conservation law yields a robust null control approach that is independent of the state of instrument and its control temporal bandwidth depends only on the brightness of the target star. It does not levy beyond state of the art stability requirements on the telescope since the telescope must be stable only over each integration window for null control.

*brian.a.hicks@nasa.gov

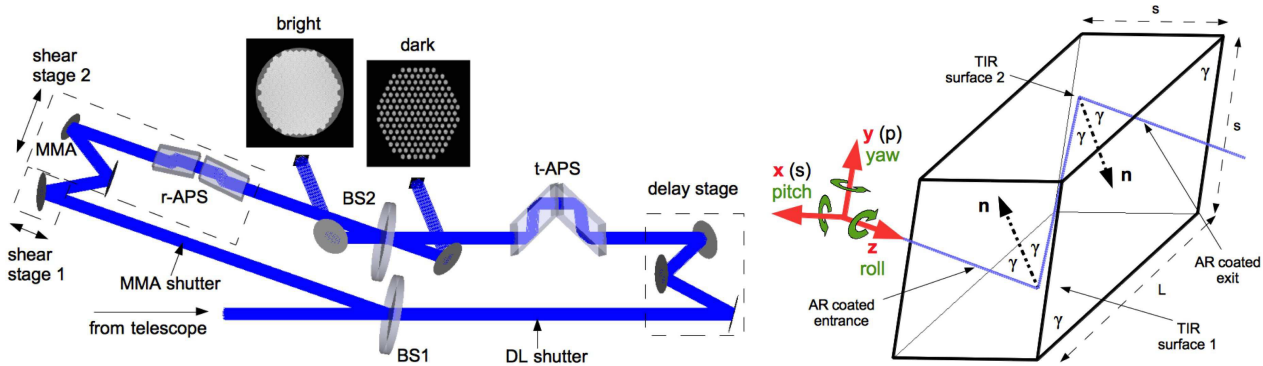


Figure 1. *Left:* The VNC model for performing sensitivity and compensation analysis used to tolerance the Fresnel rhombs APS that have been fabricated and integrated with the VNC to demonstrate 10^{-9} contrast over a 40 nm bandwidth centered at 633 nm. The APS consists of two pairs of symmetric Fresnel rhombs. The pairs are oriented orthogonally to one another in terms of their respective s- and p-planes. *Right:* The surfaces and positional angles specified in Tab. 1. The TIR surfaces are referred to as “Top” (T) and “Under” (U). The entrance and exit surfaces are referred to as “Front” (F) and “Back” (B). The non-critical side surfaces are designated “Right” (R) and “Left” (L). The most stringent requirements are placed on the parallelism of T and U and the “pitch” alignment about rhomb local x, which lies in the direction of the rhomb local s-plane.

This work describes progress toward achieving 10^{-9} contrast with the VNC at an increased spectral bandpass of 40 nm FWHM using polarized and later unpolarized sources. A tolerancing study that assumed the use of Fresnel rhombs with coated total internal reflection (TIR) surfaces and the VNC wavefront sensing and control (WFS/C) system was presented as a potential path to broadband operation.^{7,8} Here we present a summary of the design and status report on the VNC broadband demonstration following the addition of Fresnel rhombs as Achromatic Phase Shifters (APS).

2. BROADBAND COMPONENT DESIGN AND EXPECTED PERFORMANCE

Scattered starlight suppression at the level of $< 10^{-9}$ contrast has yet to be demonstrated broadband (5 – 20%) with a system that maintains high throughput ($> 10\%$) and off-axis transmission at small separation angles ($< 3\lambda/D$) with a non-circular pupil. In principle, the VNC can achieve all of these performance metrics. The key ability of broadband operation increases sensitivity for discovery and enables spectroscopic characterization of exoplanets. For a nulling interferometer (nuller) such as the VNC, operating broadband requires introducing a quasi-achromatic destructive interference condition over as large a coronagraphic region as possible in the science focal plane. For two-beam interference, this implies an achromatic π phase shift between equal amplitude nuller arms. The effect by which the VNC is attempting to accomplish this is through retardance, a difference in phase shift between polarization components introduced by an optical element or interface. Crossed Fresnel rhomb pairs provide a means by which a π phase delay can be introduced between interferometer arms,⁹ and these are presently being used to reach the VNC broadband milestone using the layout shown in Fig. 1.

Earlier design studies were performed to identify a coated TIR surface Fresnel rhomb solution using Lithosil fused silica.^{7,8} In theory, this approach could achieve an arbitrarily broad bandpass with a higher purity material, but the feasibility of achieving the layer thickness tolerances of the coating solution chosen for best performance with the least complexity was determined to be beyond the state of the art of deposition control techniques. It was later determined that a simplified design using conventional uncoated TIR surfaces with grade H4 BK7 could meet the demonstration requirements, and this approach is described here.

The most critical specification to be made is that of the TIR angle of incidence (AOI). The left panel of Fig. 2 plots TIR retardance as a function AOI derived from Fresnel equations for the central demonstration wavelength of 633 nm. Assumptions in this plot include Sellmeier dispersion for grade H4 BK7 sitting in a room temperature vacuum resulting in a nominal $55^{\circ}4'48.5''$ AOI. While the determination of the design AOI assumed a vacuum ambient medium, the demonstration is to be performed predominantly in air varying from atmospheric pressure

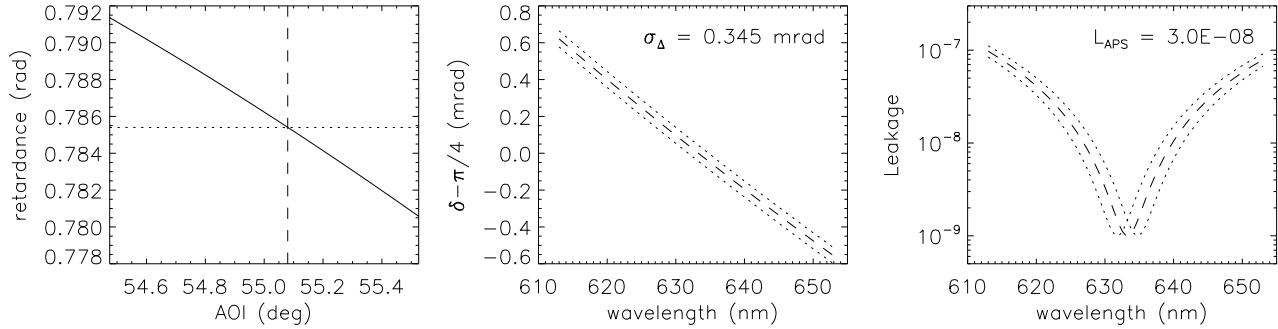


Figure 2. VNC Fresnel rhomb APS retardance curves - *left*: the AOI that gives $\pi/4$ retardance at 633 nm based on Sellmeier coefficients for BK7 at 1 atm and 293 K; *center*: change in retardance across the design bandpass at the nominal AOI (dashed) enveloped by ± 10 arcsec p-plane alignment or TIR surface parallelism errors (dotted line); *right*: Corresponding chromaticity of the null attributed solely to the slope of the Fresnel rhomb retardance for the ideal (dashed) and 10 arcsec perturbations (dotted).

to $\sim 1\%$ atmosphere inside the vibrationally isolated Vacuum Nuller Testbed.³ The affect of this assumption as it applies to the varying pressures in which the instrument will be demonstrated is a slight shift to the half wave retardance wavelength.

The central panel of Fig. 2 shows the change in retardance as a function of wavelength over the targeted 613-653 nm demonstration bandpass at the nominal angle at atmospheric pressure as well as curves that would result from ± 10 arcsec perturbances characteristic of what is expected following coarse alignment. The associated leakage curves across the demonstration bandpass is plotted in the right panel of Fig. 2 illustrating null chromaticity. A leakage floor has been added to de-emphasize the $\pi/4$ intersection that analytically equates to infinite suppression. In practice, other limits to fabrication and alignment precision give rise to asymmetric spatial and chromatic effects that raise the suppression floor. Here a floor of 10^{-9} is shown.

The calculated TIR AOI is the same as the rhomb's acute angle for normal incidence at the transmissive surfaces. Normal incidence is preferred for minimizing unwanted effects of polarization and also being able to use these surfaces for the coarse alignment effort described in Sec. 3 without needing to keep track of offsets. Two anti-reflection (AR) coating designs shown in fig3 were considered for minimizing multiple passes (i.e. etaloning) through the rhombs in the demonstration bandpass. One of the designs shown enhances reflectance by $\sim 10\times$ for the green autocollimator beam (see Fig. 7) outside of the demonstration bandpass. The other design minimizes reflectance over a broader bandpass. Either design would have met the requirement for this demonstration and choice is presented here as a point of consideration for future efforts. Based on work with uncoated engineering

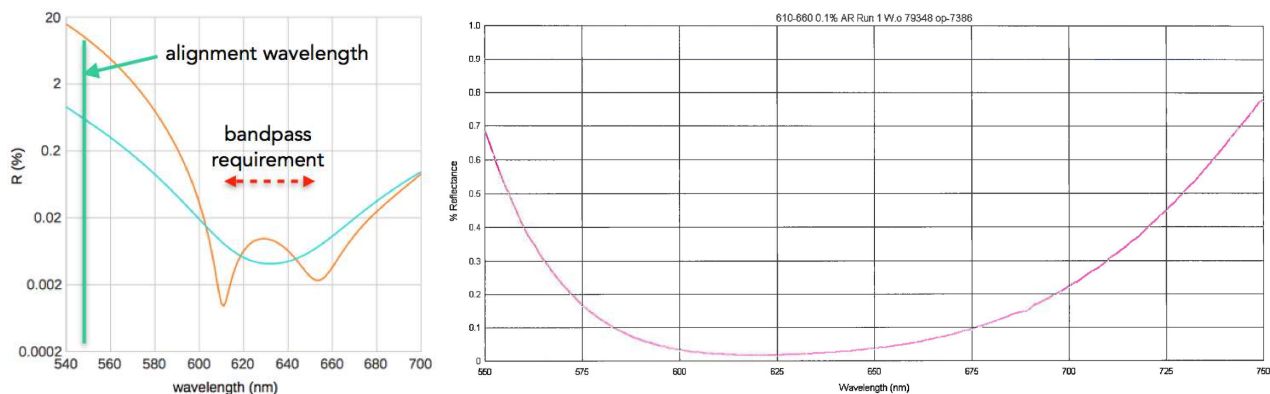


Figure 3. Multiple pass ghosts attributed to flat rhomb surfaces are mitigated by AR coatings. *Left*: Two AR coating designs considered for the fabrication of the rhombs, one with an enhancement at 543 nm outside the demonstration bandpass to aid with alignment; *Right*: Measured AR coating reflectance.

Table 1. Fresnel rhomb APS characteristics (dimensions in mm, angles in arcseconds, and surfaces in nm unless specified)

	Specification	Measurement				Comment
		FR1	FR3	FR8	FR10	
Thickness	12.3+00/-0.05 ±20 nm precision	12.28323	12.28323	12.28314	12.28314	FR1 pairs with FR8, FR3 pairs with FR10
Length (un-chamfered)	35.24+0.0/-0.1 ±50 nm precision	35.20	35.20	35.24	35.24	Precision specification not met
Entrance/exit edge length	15.0+0.0/-0.1	14.95±0.01				
Angle	55°4'48±1.0"; ±0.1 precision	55°4'48.5"±0.5"				Measurement performed on reference chuck on which parts were optically contacted for machining
TIR surface parallelism	< 0.5; ±0.1 precision	0.12	0.17	0.20	0.15	
Entrance/exit parallelism	< 0.5; ±0.1 precision	1.6	0.7	5.0	2.8	Calculated from transmitted beam deviation at 633 nm
Right angle errors	±1.0' from 90°	< 0.5'	< 1.0	< 1.0	< 0.5	
P-V WFE	< 43 (< λ/15 at 633 nm)	12, 20, 10, 11	11, 24, 12, 9	16, 31, 10, 17	21, 14, 10, 24	F, B, T, U surfaces; see Fig. 5
RMS WFE	< 13 (< λ/50 at 633 nm)	2, 4, 1, 2	1, 4, 2, 1	3, 4, 1, 3	4, 2, 1, 4	F, B, T, U surfaces; see Fig. 5
P-V WFE	< 159 (< λ/4 at 633 nm)	103 114	95 109	155 109	122 93	R, L alignment surfaces
RMS surface roughness	< 1	0.8 (F) 0.9 (F), 0.8 (B)				
Scratch/Dig	10/5	10/5				
Entrance/exit reflectance	$R_{avg} < 0.1\%$, 613-653 nm	< 0.1%				See Fig. 3

rhombs, it was determined that the return from the lesser green reflectance would still be detectable and the non-oscillatory solution that achieves $R < 0.1\%$ over a broader bandpass was selected for the demonstration pieces.

The other basic geometric specification of the Fresnel rhombs is driven primarily by the size of and distance to the instrument's deformable mirror, which lies in a pupil. Not being in a pupil, other factors that determine the size of the rhombs' transmissive clear aperture and ultimately the scale of each rhomb and pair include the prism angle (γ in the right panel of Fig. 1), as well as on-sky field of view and telescope to coronagraph magnification. The clear aperture for this demonstration was sized to accommodate not just the present, but also forthcoming DMs with the same Fresnel plane spacing of the present layout.

Rhomb fabrication tolerances were determined from a study performed using the model shown in Fig. 1. Ultimately, perturbing each feature individually and in groups was performed "by hand" followed by simulated compensation using piezoelectric transducer (PZT) fine positioners and a delay stage in order to determine tolerances. Phenomena considered in the study included refraction and chromatic beam shear, TIR retardance, and bulk dispersion. Errors in prism facet angles were compensated by the modeled all-reflective VNC delay line modified Mach-Zehnder "W" shown schematically in Fig. 1 and in a photo of the actual setup in the left panel of Fig. 7. Tolerances are summarized in Tab. 1 along with the measured data for the first set of fabricated demonstration-quality Fresnel rhombs, serialized as FR1, FR3, FR8, and FR10. The fabrication tolerances of the rhomb facets and their positions relative to one another and the instrument are on the order of about an arcsecond to achieve 10^{-9} final contrast. The most stringent requirement is on the parallelism and symmetry of the TIR surfaces.

In order to meet symmetry requirements, the rhombs were fabricated using a dicing approach in order to match bulk path lengths between pieces and achieve the best possible parallelism for the critical optical surfaces (F,B,T, and U identified in the caption of Fig. 1). Parallelism is key to limiting refractive polarization-based

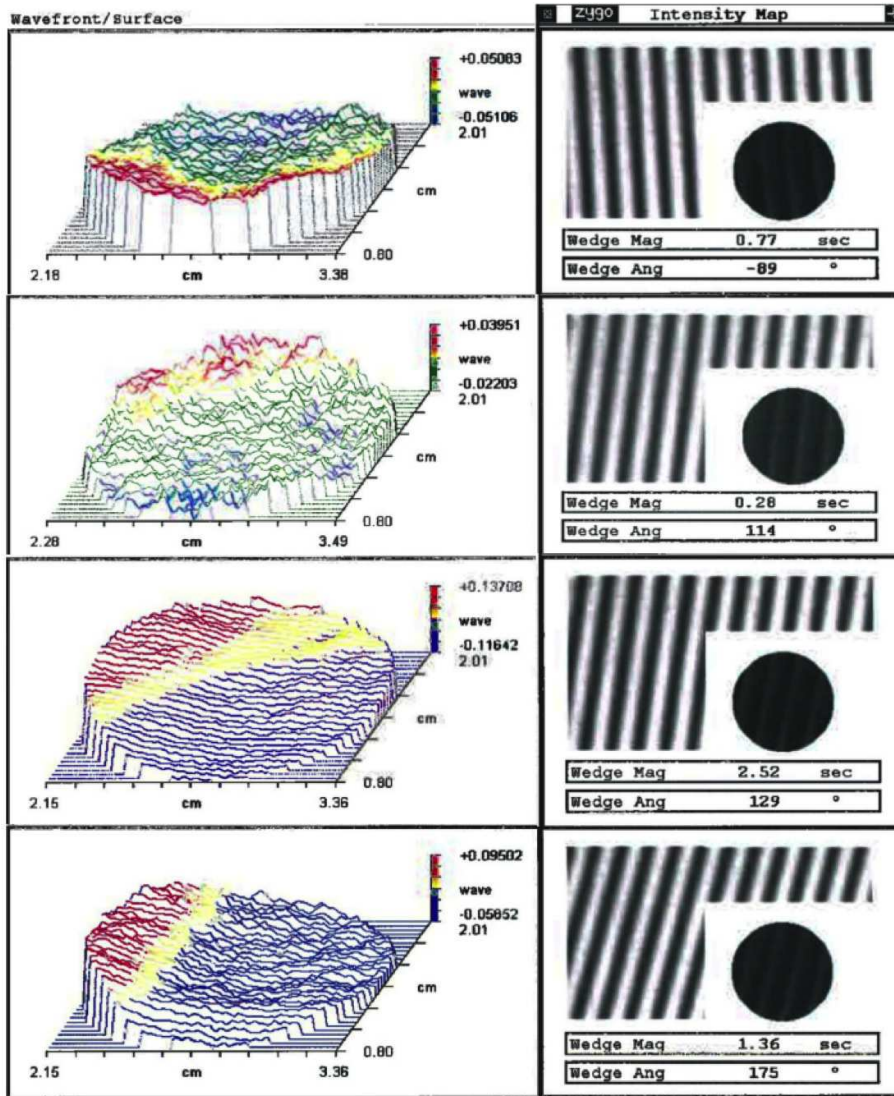


Figure 4. A measure of beam deflection passing through each rhomb. A Zygo was used to compare the path through air between two reference surfaces and through each rhomb. The fringe pattern in the “L” shaped area is the reference, the much dimmer fringe pattern in the circular area is through the rhomb. Because the rhombs are waveplates, and the Zygo uses polarized light, the visibility of the fringes in the circular rhomb portion is diminished. The reported values are the sum of entrance and exit surface (F and B) parallelism and TIR surface (T and U) parallelism parallelism. The parallelism of the TIR surfaces is measured directly.

wavefront asymmetries at the entrance and exit faces (F and B), and more importantly, achieving chromatically symmetric $\pi/4$ retardance. The transmissive and TIR surface interface wavefront effects scale according to Fresnel equations. Example effects of the latter are plotted in Fig. 2.

Matching path lengths between arms is critical for minimizing differential bulk dispersion starlight leakage that scales as

$$L_{\delta z}(\lambda) \propto \left[2\pi\delta z \left(\frac{n(\lambda)}{\lambda} - \frac{n(\lambda_o)}{\lambda_o} \right) \right]^2 \quad (1)$$

where δz is the physical path difference for a given ray through rhomb pairs and the control system minimizes field asymmetry for some wavelength λ_o . While the expression is simple, the actual value of δz is pupil position dependent and a complex interplay of not only errors in parallelism, but also slight misalignment of the rhombs relative to the nuller axis, which gives rise to refraction. The actual determination of the pupil- and wavelength-dependent path error may be determined using a calculus of variations approach using measured errors and assumed perfect alignment, or numerically using Monte Carlo methods to determine confidence intervals for expected performance given a set of random alignments with the same set of measurements. In theory, extreme care in registering independent wedge magnitudes and angles could be used to find a best possible alignment of the four rhombs in a given set inside the interferometer. This effort is restricted to using matched pairs based

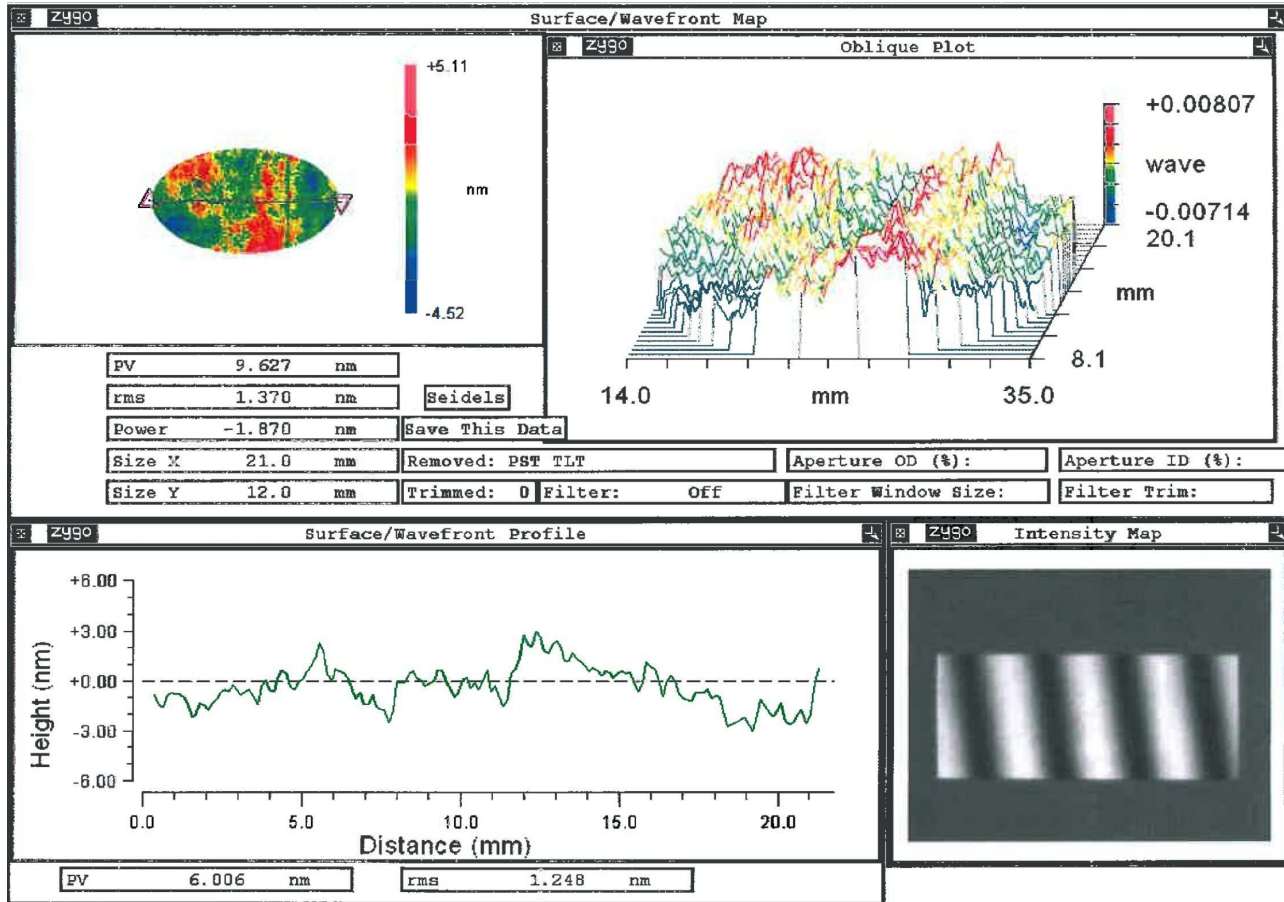


Figure 5. The measured RMS wavefront error of the rhomb optical surfaces were measured to be 3 – 10× better than specified. Shown here is sample surface data for the FR3 “Under” TIR surface.

on the dicing as indicated in Tab. 1.

The incorporation of active fine positioners makes it possible to split the error in parallelism of TIR surfaces at the potential cost of adding more refraction at one or both transmissive surfaces. In theory, designing to have this sort of control for each individual rhomb (as opposed to being in contacted pairs) allows for better performance. The challenge lies in the design of tiered alignment stages that afford both coarse positioning and fine control between the rhombs, between the pairs, and relative to the instrument. One simplification made in this effort was to only use coarse positional control for one of the rhombs, making it a “keystone” to which the other rhombs are fine-aligned. The fine alignment is performed using PZT stages with three actuators that allow for bidirectional control of pitch and yaw as defined in Fig. 1. The procedure for performing this alignment is described in more detail in Sec. 3.

Considering general top level error budgeting effects typically associated with phase, amplitude, and polarization asymmetries, the contrast in the image plane may be approximated as¹⁰

$$C(\rho) \sim \frac{\sigma_{DH}^2/\sigma_T^2}{1 + \frac{\pi^4}{8}|\rho|^3} \left(\frac{\sigma_\phi^2}{4} + \frac{\sigma_I^2}{16} + \frac{\sigma_\psi^2}{4} \right) \quad (2)$$

where σ_{DH}^2 is the wavefront variance contained within the spatial frequencies corresponding to the image plane dark hole and σ_T^2 is the total wavefront variance at all spatial frequencies given by the 2D integral of the PSD over all spatial frequencies. The terms $\{\sigma_\phi^2, \sigma_I^2, \sigma_\psi^2\}$ are the total variances, i.e. at all spatial frequencies, for

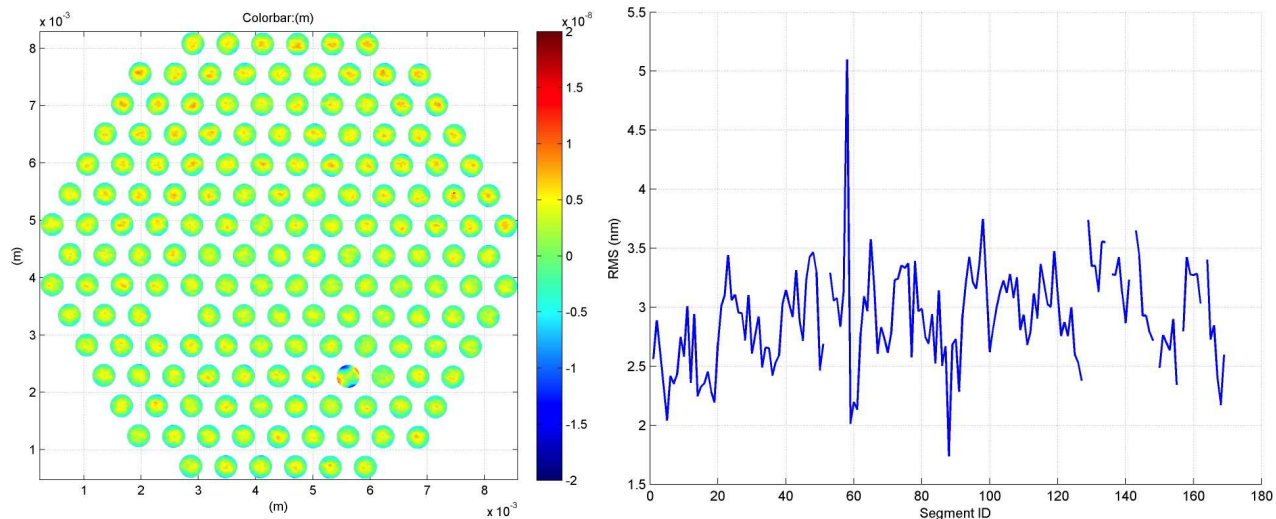


Figure 6. *Left*: Measured 400 μm circular subaperture surface data of the Iris, AO PTT489 DM used to reach the narrowband milestone.³ This same DM is presently being used to begin work towards reaching the broadband milestone. Two out of five segments that are masked out by the Lyot stop are apparent, one as a missing segment, the other showing an astigmatic pattern. *Right*: A corresponding plot of the RMS surface error within each circular subaperture. An array of single mode fibers could be used to further reduce the correlated wavefront error over the low spatial frequencies corresponding to the dark region of highest contrast targeted by the wavefront control algorithm.^{3,10}

phase errors, intensity errors, and polarization errors, respectively. Calculating the fractional power of these errors within the spatial frequency range of interest enables specification of the suppression that needs to be achieved in the pupil (proxied as leakage in Fig. 2), and the total RMS surface figure error, coating uniformity, and polarization variation. Each of these terms is affected not just by the APS asymmetries, but also the deformable mirror (DM) itself used to correct these and all other asymmetries present in the interferometric cavity.

The VNC uses a hexagonally-packed segmented DM¹¹ for phase control across the instrument beam attributed to coating and polishing defects introduced by each element in the optical train. The approach to WFS/C is described in more detail in other recent works.^{3,8} Here it suffices to state that wavefront control is performed in such a way to balance phase, amplitude, and polarization effects to optimize contrast within a range of spatial frequencies corresponding to the dark hole region of the science image plane. The optical surface quality of the DM being used in the present broadband demonstration is presented in Fig. 6.

A segmented DM is also referred to as a multiple mirror array (MMA) to distinguish it from a continuous facesheet DM, which has actuators that are inherently coupled with their nearest neighbors. The largest optimized dark region (“dark hole”) size that can be achieved with a continuous facesheet DM scales as a Nyquist limited controller, but it does not quite reach the $N/2$ limit. Assuming a 128×128 Cartesian grid, the Nyquist limit would give 64 cycles per aperture (cpa), but the point spread function (PSF) has a $\sim \rho^3$ tail. As such, when optimizing the dark hole from $2 - 64\lambda/D$ the flux outside of $64\lambda/D$ spills some flux back into the dark hole due to the sum of all the tails since each speckle is really a PSF. This becomes a limiting factor on contrast and it depends on the power spectral distribution of the wavefront error.

A segmented DM, however, fits both local piston and local slope. Breaking the surface into Fourier components fitted at each point along a sine wave gives a smaller RMS error to a fit.¹² Thus, in the 1D case, given a 64 segment DM, corrections can be made out to 64 cpa. Achieving the same correction with a continuous facesheet DM requires 128 actuators. Adding the second dimension does not yield the same gain since three points defining a plane must be fit to a 2D sine wave. The hexagonal geometry complicates analytical calculations of fitting errors and in general the wavefront control problem is addressed numerically.

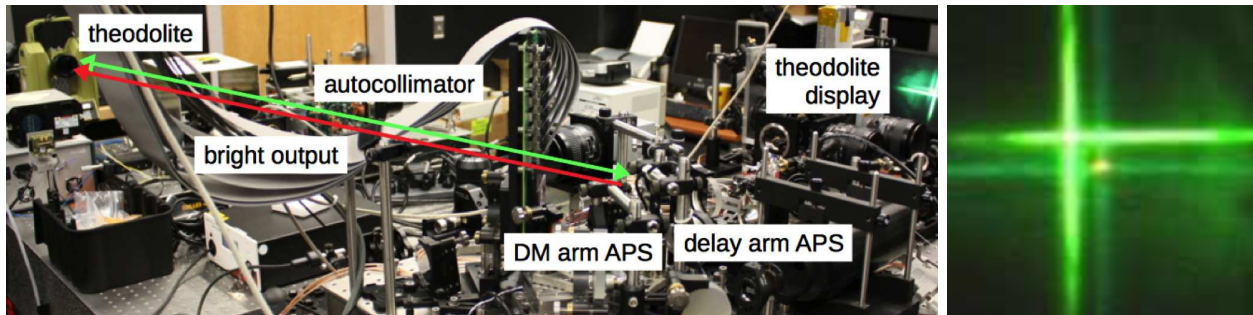


Figure 7. *Left:* the setup for aligning each APS rhomb to the VNC instrument null axis. A similar configuration is used to observe the parallelogram (L and R) sides of the rhombs to set roll and yaw as defined in Fig. 1. *Right:* alignment theodolite detector snapshot showing returns coming from the entrance and exit surfaces of each APS rhomb with the fine positioning piezos powered at midrange. The bright crosshairs are an internal artifact of the autocollimator source and the fainter crosshairs are the returns from the rhombs. The returns from all rhomb faces (8 total) are stacked appearing as a single return. The central red spot is the VNC source through the delay arm indicating the null axis to which the rhombs are aligned.

3. CURRENT STATUS AND FORTHCOMING WORK

As of the time of writing, the demonstration APS have been successfully installed into the VNC twice. While this is a process that involves significant care in handling, the coarse alignment procedure can be accomplished with a combination of standard tools including a Zygo interferometer and theodolite which are each used to achieve ~ 10 arcsec precision. The first step is to align the rhombs individually using coarse actuation with the PZTs set to midrange in order to align them as a half wave pair. The L and R parallelogram faces that are surfaces that are not traversed by the nuller path constrain roll and yaw, and square entrance and exit faces (F and B) are used to set the critical pitch angle. The parallelism internal to the rhombs is better than what can be resolved by the theodolite, and this is evidenced in Fig. 7 where the crosshairs from the aligned APS returns (eight surfaces total) are all superimposed.

Removing a fold mirror that steers the bright output through an adjustable focus lens to the wavefront sensor is one example of a simple modification that can be made to accommodate coarse alignment of the rhombs. After such an adjustment is made, it is straightforward to replace the optic and realign to the digital mask that flags pixels for consideration within DM segment subapertures. Alternatively, small perturbations to this alignment that can be accommodated by regenerating the digital mask, which also allows for anamorphic corrections. Verification of digital mask correspondence is performed by either varying control voltages for segments randomly or by specified amounts. An intermediate state of WFS digital mask verification is shown in Fig. 8 in the form of ensemble phase shifting performed to match the reference wavefront of the nuller delay arm.

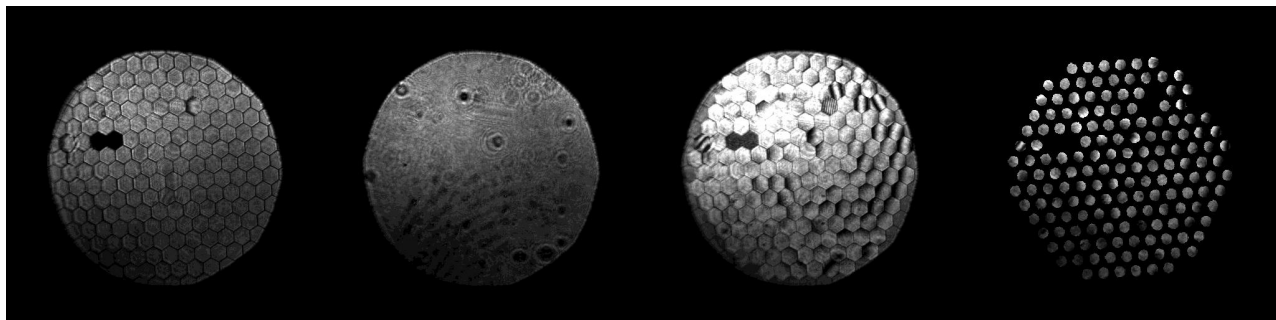


Figure 8. *Left to right:* Wavefront sensor frames recorded in the VNC bright channel for conditions of the reference arm shutter closed, the DM arm shutter closed, both shutters open, and both shutters open with the digital mask applied. The digital mask corresponds to the physical Lyot mask. Non-zero values are used to compute piston, tip, and tilt for each segment.

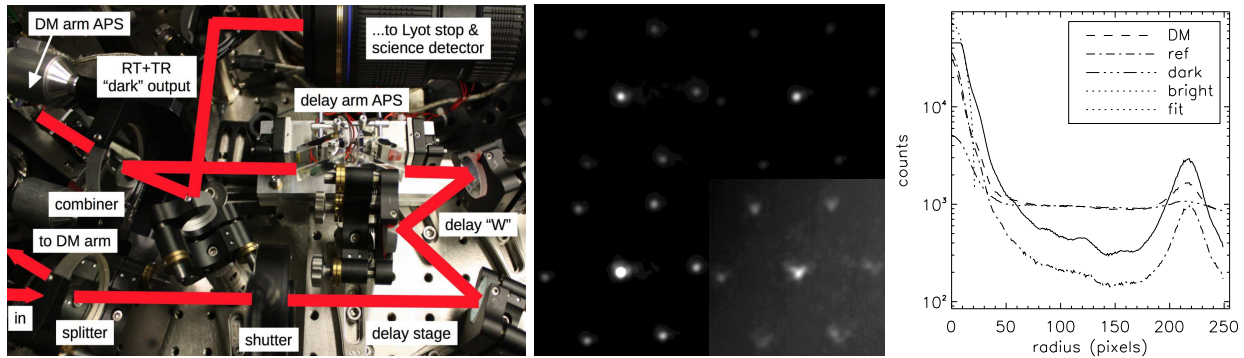


Figure 9. *Left:* The delay arm of the VNC breadboard with broadband demonstration additions including the Achromatic Phase Shifter (APS) Fresnel rhombs mounted on hybrid coarse and piezo-actuated individual and pair stages. *Center clockwise from top left and right:* single frames recorded in the dark channel focal plane observed without mechanical stabilization in air with the delay shutter closed (“DM”), the DM arm shutter closed (“ref”), both shutters open near null (“dark”), and both shutters open with the only perturbation being a 2V adjustment to the active DM arm APS fine pitch actuator (“bright”) along with radial averages of the focal plane frames following scalar bias subtracted. The bias is the mean value of a 50×50 pixel dark patch in the nulled frame. A Gaussian fit to the bright central core is also shown to extend beyond the sCMOS saturation level.

A similar minor realignment is performed for the physical Lyot mask in the dark output after replacing a relay lens that is removed in order to install the delay arm APS. This lens is shown in the left panel of Fig. 9.

The functionality of the rhomb fine PZT positioners is verified by monitoring a combination of responses in theodolite or instrument fringe observation modes. The faint crosshairs shown in Fig. 7 are superimposed (out of demonstration band) returns from the AR coated transmissive APS faces. Both pitch and/or yaw (see Fig. 1) can be observed to change by actuating any one of three PZT amplifier voltages. Changing all three voltages for a single rhomb fine control stage by the same amount introduces piston, which has no observable effect since this merely displaces the bulk propagation path relative to the ambient path. It is noted that fringes are sensitive to rhomb pitch adjustment, whereas adjusting pure yaw is best observed in theodolite mode. Control of broadband performance is achieved through the VNC control software interface to PZT amplifiers. A very basic demonstration of the APS fine control is evidenced in Fig. 9 where a change in $\sim 2V$ on a pitch actuator introduces brings the dark output PSF core out of a nulled state into saturation. Also shown are the PSFs corresponding to one beam in the interferometer or the other. Radial averages of these single frames are shown on a log scale in the right panel of Fig. 9. These frames were recorded in air with no mechanical isolation.

Results of alignment checkouts in air have indicated that the VNC and its broadband upgrades are ready to be moved to the Vacuum Nuller Testbed (VNT)³ chamber to begin the final phase of this demonstration. In order to achieve the IWA of $2\lambda/D$, the wavefront will need to be sensed and controlled at spatial frequencies of ~ 2 cpa in closed loop to hold the mean contrast at 10^{-9} . As was previously achieved with the narrow band demonstration, the goal of the broadband milestone is to demonstrate that the mean contrast can be held for > 1000 seconds, a stability requirement that traces to the exposure times required to search, detect, and perform spectroscopic characterization of exoplanets. Conclusion of this broadband milestone will validate the VNC sensing algorithms employing the bright and dark outputs, and the control algorithms for the MMA. The results will be repeated emulating a slew to a new target for a flight mission.

ACKNOWLEDGMENTS

The authors acknowledge support from NASA/Goddard Space Flight Center Internal Research and Development (IRAD), and from the NASA Strategic Astrophysics Technology (SAT) Technology Development for Exoplanet Missions (TDEM) program. Brian Hicks is a Fellow of the NASA Postdoctoral Program administered by Oak Ridge Associated Universities. The rhombs described in this work were fabricated by LightMachinery, Inc., with polishing credited to Vaz Zastera, and fluid jet corrections and measurements performed by Jakub Cieniak.

REFERENCES

- [1] Clampin, M., Melnick, G., Lyon, R., Kenyon, S., Sasselov, D., Tolls, V., Ford, H., Golimowski, D., Petro, L., Hartig, G., Sparks, W., Illingworth, G., Lin, D., Seager, S., Weinberger, A., Harwit, M., Marley, M., Schneider, J., Shao, M., Levine, M., Ge, J., and Woodruff, R., “Extrasolar planetary imaging coronagraph (EPIC),” *Proc. SPIE* **6265** (July 2006).
- [2] Lyon, R. G., Clampin, M., Woodruff, R. A., Vasudevan, G., Ford, H., Petro, L., Herman, J., Rinehart, S., Carpenter, K., and Marzouk, J., “Balloon exoplanet nulling interferometer (BENI),” *Proc. SPIE* **7440** (Aug. 2009).
- [3] Lyon, R. G., Clampin, M., Petrone, P., Mallik, U., Madison, T., and Bolcar, M. R., “High contrast vacuum nuller testbed (VNT) contrast, performance, and null control,” *Proc. SPIE* **8442** (Sept. 2012).
- [4] Content, D. A., Armani, N. V., Baker, C. L., Jackson, C. E., Kahle, D. M., Kruk, J. W., Lehan, J. P., Melton, M. E., Mentzell, E., Miko, J. J., Palace, D. J., Pasquale, B. A., Peabody, H. L., Smith, B. S., Smith, W. F., Stewart, J. W., Vaughn, D. A., Waczynski, A., and Wallace, T. E., “Wide field instrument preliminary design for the Wide Field InfraRed Survey Telescope,” *Proc. SPIE* **8860** (Sept. 2013).
- [5] Postman, M., Brown, T., Sembach, K., Giavalisco, M., Traub, W., Stapelfeldt, K., Calzetti, D., Oegerle, W., Michael Rich, R., Phillip Stahl, H., Tumlinson, J., Mountain, M., Soummer, R., and Hyde, T., “Advanced Technology Large-Aperture Space Telescope: science drivers and technology developments,” *Optical Engineering* **51**, 011007 (Jan. 2012).
- [6] Dalcanton, J. and Seager, S., “From cosmic birth to living earth: The future of uvoir space astronomy,” tech. rep., Association of Universities for Research in Astronomy (2015).
- [7] Bolcar, M. R. and Lyon, R. G., “Approaches for achieving broadband achromatic phase shifts for visible nulling coronagraphy,” *Proc. SPIE* **8445** (July 2012).
- [8] Hicks, B., Lyon, R., Bolcar, M., Clampin, M., and Petrone, P., “High-contrast visible nulling coronagraph for segmented and arbitrary telescope apertures,” *Proc. SPIE* **9143** (2014).
- [9] Mawet, D., Hanot, C., Lenaers, C., Riaud, P., Defrère, D., Vandormael, D., Loicq, J., Fleury, K., Plessier, J. Y., Surdej, J., and Habraken, S., “Fresnel rhombs as achromatic phase shifters for infrared nulling interferometry,” *Optics Express* **15**, 12850 (Sept. 2007).
- [10] Clampin, M., Lyon, R., Petrone III, P., Mallik, U., Bolcar, M., Madison, T., and Helmbrecht, M., “Visible nulling coronagraph technology maturation High contrast imaging and characterization of exoplanets,” tech. rep., NASA/Technology Development for Exoplanet Missions Final Report, JPL Document D-80950, https://exep.jpl.nasa.gov/technology/Clampin_Report_FINAL.pdf (2013).
- [11] Helmbrecht, M. A., He, M., and Kempf, C. J., “High-actuator-count MEMS deformable mirrors,” *Proc. SPIE* **8725** (May 2013).
- [12] Sweatt, W. C., “Reduction of Zernike wavefront errors using a micromirror array,” *Optical Engineering* **44**, 098001 (Sept. 2005).